Published online 12 July 2022 *Nucleic Acids Research, 2022, Vol. 50, No. 13* ***7493–7510***
https://doi.org/10.1093/nar/gkac603

Selective pericentromeric heterochromatin dismantling caused by TP53 activation during senescence

Aaron Mendez-Bermudez[1,2], Liudmyla Lototska[2], Melanie Pousse[2], Florent Tessier[2], Oliver Croce[2], Chrysa M. Latrick[2], Veronica Cherdyntseva[3], Joe Nassour[4], Jiang Xiaohua[5], Yiming Lu[1], Corinne Abbadie[4], Sarantis Gagos[3], Jing Ye[1,*] and Eric Gilson[1,2,6,*,†]

[1]Department of Geriatrics, Medical center on Aging of Shanghai Ruijin Hospital, Shanghai Jiaotong University school of Medicine; International laboratory in Hematology, Cancer and Aging, Pôle Sino-Français de Recherches en Sciences du Vivant et Génomique, Rui Jin Hospital, Shanghai Jiao Tong University School of Medicine, Shanghai, China; CNRS/INSERM/University Côte d'Azur, [2]Université Côte d'Azur, CNRS, INSERM, IRCAN, Faculty of Medicine Nice, France, [3]Laboratory of Genetics, Center of Experimental Medicine and Translational Research, Biomedical Research Foundation of the Academy of Athens, Greece, [4]Univ. Lille, CNRS, Inserm, CHU Lille, Institut Pasteur de Lille, UMR9020-U1277, CANTHER, Cancer Heterogeneity Plasticity and Resistance to Therapies, F-59000 Lille, France, [5]School of Biomedical Sciences, The Chinese University of Hong Kong and [6]Department of medical genetics, CHU, Nice, France

Received December 13, 2021; Revised June 17, 2022; Editorial Decision June 24, 2022; Accepted July 01, 2022

ABSTRACT

Cellular senescence triggers various types of heterochromatin remodeling that contribute to aging. However, the age-related mechanisms that lead to these epigenetic alterations remain elusive. Here, we asked how two key aging hallmarks, telomere shortening and constitutive heterochromatin loss, are mechanistically connected during senescence. We show that, at the onset of senescence, pericentromeric heterochromatin is specifically dismantled consisting of chromatin decondensation, accumulation of DNA breakages, illegitimate recombination and loss of DNA. This process is caused by telomere shortening or genotoxic stress by a sequence of events starting from TP53-dependent downregulation of the telomere protective protein TRF2. The resulting loss of TRF2 at pericentromeres triggers DNA breaks activating ATM, which in turn leads to heterochromatin decondensation by releasing KAP1 and Lamin B1, recombination and satellite DNA excision found in the cytosol associated with cGAS. This TP53–TRF2 axis activates the interferon response and the formation of chromosome rearrangements when the cells escape the senescent growth arrest. Overall, these results reveal the role of TP53 as pericentromeric disassembler and define the basic principles of how a TP53-dependent senescence inducer hierarchically leads to selective pericentromeric dismantling through the downregulation of TRF2.

INTRODUCTION

Aging is a multifactorial process that results in progressive loss of regenerative capacity and tissue function, while simultaneously promoting the development of a large panel of age-related diseases (1). Evidence suggests that cellular senescence is a basic aging process that is pivotal to drive these changes (2). Senescence is a permanent non-dividing cellular state triggered by numerous stressors leading to the activation of the tumor-suppressing pathways p53/p21^{WAF1} and p16^{INK4a}/pRB, as well as dramatic cellular changes including chromatin remodeling, metabolism switch, gene expression alterations and the secretion of inflammatory cytokines, growth factors, proteases and other molecules consisting of the senescence-associated secretory phenotype (SASP). Among the numerous changes in chromatin structure occurring during senescence, the dynamics of heterochromatin are complex: while localized regions

*To whom correspondence should be addressed. Fax: +33 49337092; Email: eric.gilson@unice.fr
Correspondence may also be addressed to Pr. Jing Ye. Tel: +86 13585625087; Fax: +86 21 64671676; Email: yj11254@rjh.com.cn
†Lead author.
Present address: Joe Nassour, The Salk Institute for Biological Studies 10010 North Torrey Pines Rd. La Jolla, CA 92037 USA.

of heterochromatin known as senescence-associated heterochromatic foci (SAHF) are formed in some types of senescent cells (3), constitutive heterochromatin vanishes in most if not all types of senescence leading to its transcriptional derepression and contributing to aging (4–6). Constitutive heterochromatin is found in all cell types at pericentromeres, telomeres/subtelomeres, retrotransposons and endogenous retroviruses and relies on the histone methyltransferases (SUVAR39H1/2 and SETDB1) to establish H3K9me3 chromatin domains covered by arrays of HP1 proteins (7).

Although several effectors of heterochromatin remodeling have been identified (8–12), how they are causally connected to senescence stressors remains unknown. Here, we investigate the relationship linking two key aging hallmarks, telomere shortening and constitutive heterochromatin loss, and ask how they are mechanistically connected during aging. For this, we designed a time-course experiment starting from young primary to replicative senescent cells that allowed us to uncover the central role of a TP53–TRF2 axis driving a selective and severe constitutive heterochromatin dismantling, including the excision of pericentromeric DNA repeats triggering a cGAS-STING response in the cytosol. These results show how several aging hallmarks (here senescence, telomere shortening, DNA damage response, heterochromatin loss and inflammation) can be hierarchically connected. Our findings further argue that the predicted heterochromatin information loss observed during aging is not a chaotic event but a programmed mechanism starting from TP53 activation.

MATERIALS AND METHODS

Cell lines

Human primary MRC-5 and WI-38 cells were obtained from the ATCC. IMR-90 cells were a gift from the Jean-Marc Lemaitre lab, while the sh*TERF2*-inducible HeLa cell line was a gift from the Joachim Lingner lab. All cell lines used in this study were grown in DMEM supplemented with 10% fetal calf serum. Primary cell lines were grown at 5% oxygen. All cell lines were routinely tested for mycoplasma contamination.

Reagents: antibodies

The following primary antibodies were used for immunofluorescence: anti-53BP1 (Novus Biologicals, NB100-305), anti-TRF2 (Novus Biologicals IMG-124A), anti-pATM (ser1981) (Cell Signaling Technology, 4526), anti-KAP1 (abcam, ab22553), anti-Lamin B1 (abcam, ab16048), anti-H3K9me3 (abcam, ab8898) and anti-cGAS (D1D3G) (Cell Signaling Technology, 15102). For western blotting: anti-TRF2 (Novus Biologicals, NB110-57130), anti-TRF1 (Santa Cruz Biotechnology, sc-6165), anti-Pot1 (Abcam, ab21382), anti-TPP1 (Abcam, ab195234), anti-TIN2, anti-RAP1 (Bethyl, A300-306A), anti-p53 (Abcam, ab131442), anti-actin, anti-GAPDH (Novus Biologicals, NB100-56875), anti-$p21^{CIP1}$ (Abcam, ab16767), anti-$p16^{INK4A}$ (Abcam, ab 554079). Antibodies used for ChIP slot blot and ChiP-seq experiments: anti-γH2A.X (Abcam, ab2893), anti-H3K9me3 (Upstate, 07-442), anti-Lamin B1 (abcam, ab16048) and anti-KAP1 (abcam, ab22553). Secondary antibodies were: goat anti-rabbit Alexa 488 antibody (111-545-144; Jackson Immunodetect), goat anti-mouse Alexa 488 antibody (115–545-146; Jackson Immunodetect), HRP goat anti-mouse IgG (Vector Laboratories, PI-2000) and HRP goat anti-rabbit IgG (Vector Laboratories, PI-1000).

Senescence and proliferation assay

To detect senescence-associated β-galactosidase (SA-β-Gal) activity in cultured cells, the Senescence Detection Kit (Abcam, ab65351) was used according to the manufacturer's instructions. To assess for cellular proliferation, 10 μM EdU was added to the culture for 24 h at 1 μM final concentration. EdU was detected using the Click-iT EdU Alexa Fluor 647 Imaging Kit (Thermo Scientific, C10340).

Comet-FISH assay

For each condition, around 5000 cells were embedded in 0.5% low-melting agarose dissolved in 1× PBS. The suspension was immediately laid onto comet slides (4250–200-03, Trevigen). Agarose was allowed to solidify at 4°C for 20 min and the comet slides were then immersed in pre-chilled lysis solution (2.5 M NaCl, 100 mM EDTA, 10 mM Tris and 1% Triton, pH 10) at 4°C for 90 min in the dark. Next, the comet slides were placed in a horizontal electrophoresis unit and allowed to equilibrate in 0.5× TBE buffer (pH 8) for 5 min at 4°C in the dark. The migration was performed at 40 V for 20 min. The slides were then placed in 100% ethanol for 30 min at 4°C and denatured in 0.5 M of NaOH for 25 min. Finally, the slides were dehydrated in an ascending series of ethanol solutions (50%, 70% and 100% for 5 min each) and air-dried.

Hybridization with Satellite III (Sat III), telomere and centromere PNA probes (Panagene) was performed at RT for at least 2 h in 70% formamide, 10 mM Tris pH 7.2 and 1% blocking solution (Roche). Following hybridization, the slides were washed with a solution containing 50% formamide and 10 mM Tris pH 7.2 for 30 min, followed by a 10 min wash in a solution of 50 mM Tris pH 7.5, 150 mM NaCl and 0.05% Tween-20. Slides were left to air dry for 30 min and the DNA was stained with either YOYO-1 or propidium iodide for 10 min.

For analysis, the tail moment (tail length × DNA in the tail / total DNA) was recorded for each comet (60–80 cells) using the Tritek Comet Score freeware. The PNA signal was visualized with a Zeiss epi-fluorescence microscope. The student's t-test was used for statistical analysis.

Genomic DNA extraction and Southern blotting

In brief, high molecular weight DNA was extracted by lysing the cells in a 100 mM Tris–HCl pH 7.5, 100 mM NaCl, 10 mM EDTA, 1% Sarkosyl solution. An initial incubation of 20 min with 50 μg/ml RNase was followed by 500 μg/ml proteinase K for 6 h at 55°C. The samples were then subjected to phenol/chloroform extraction and ethanol precipitation. DNA was digested with HindIII, and about 2

μg was electrophoresed in a CHEF-DR III pulse-field electrophoresis apparatus (Bio-Rad Laboratories) in recirculating 0.5× TBE buffer at 14°C. Electrophoresis was performed for 16 h using 6 V/cm and 50–90 s switch time. The gel was rinsed and stained with ethidium bromide to visualize the DNA and Southern blotting was carried out using standard methods. The Southern blot membrane (Hybond N+, GE Healthcare) was hybridized to ^{32}P-αdCTP-labeled probes in Church buffer at 65°C. The signal was visualized using a phosphor imager scanner (Typhoon; GE Healthcare) and analysis was performed using Image Quant TL software (GE Healthcare).

Chromatin orientation fluorescence in situ hybridization

CO-FISH was carried out as described previously (13) with some modifications. Briefly, a mix of BrdU:BrdC (3:1) was added to the media of MRC-5 for 20 h. The next day, metaphase spreads were generated using standard methods. Slides containing metaphase spreads were treated with 0.5 mg/ml RNaseA for 10 min at 37°C and stained with 0.5 ug/ml Hoechst 33258 for 15 min at room temperature. Then, slides were placed in a plastic tray containing 2× SSC and exposed to 365 nm UV light for 30 min. Incorporated BrdU/BrdC was removed with 800 U of exonuclease III (Promega) followed by dehydration with increasing concentrations of ethanol. Hybridization of Sat III strand-specific PNA probes (Cy3-OO-TTCCATTCC ATTCCATTCCA and FAM-OO-TGGAATGGAATGG AATGGAA) was performed sequentially for 2 h each. The removal of unspecific PNA probe was done by washes with 70% formamide, 10 mM Tris pH 7.2 and 50 mM Tris pH 7.5, 150 mM NaCl, 0.05% Tween. Finally, cells were preserved in a mounting solution with DAPI (Vectashield, Vector Laboratories). Quantification was performed by calculating the percentage of chromosomes containing a pattern of staining different from a single-side PNA signal. This does not discriminate between stable inversion events present in those regions.

Proximity ligation assay (PLA)

Cells were grown on glass coverslips and fixed with 2% formamide for 15 min followed by permeabilization with 0.25% triton for 15 min at room temperature. Next, the hybridization of a biotinylated Sat III PNA probes (Bi otin-OO-TTCCATTCCATTCCATTCCA) was performed for at least 2 h followed by washes with 70% formamide, 10 mM Tris pH 7.2 and 50 mM Tris pH 7.5, 150 mM NaCl, 0.05% Tween. Subsequently, the slides were blocked using the Duolink PLA reagents (Sigma) following the manufacturer's recommendations. PLA was then performed using a combination of rabbit and mouse antibodies: mouse anti-PCNA (P8825, Sigma), mouse anti-KAP1 (ab22553, Abcam), rabbit anti-LaminB1(ab16048, Abcam), mouse anti-biotin (B7653, Sigma) and rabbit anti-biotin (5597, CST). Antibody incubation was performed overnight at 4°C followed by PLA detection using the Duolink *in situ* detection kit (Sigma).

Multicolor FISH (M-FISH)

Chromosome spreads were prepared by arresting actively dividing MRC-5 cultures using 50 ng/ml colcemid (KaryoMAX, Invitrogen) for 2 h at 37°C. Afterward, trypsinized cells were incubated with hypotonic solution (75 mM KCl) for 15 min at 37°C, fixed with ice-cold methanol:glacial acetic acid (3:1), and spread on slides. mFISH was performed using the 24XCyte kit (MetaSystems Probes) according to the manufacturer's instructions. Stained metaphase chromosomes were visualized on the Zeiss Axiovert Z2 epi-fluorescent microscope and analyzed using the metasystem ISIS software.

Microsatellite instability

Microsatellite instability was assayed by PCR amplification using the Platinum hot-start PCR master mix (ThermoFisher). The PCR products were loaded into a microfluidic chip for DNA (Agilent DNA 1000 kit) and the analysis was performed with the 2100 Bioanalyzer instrument (Agilent).

Lentivirus infection and siRNA transfection

si*TERF2*, si*TRIM28* and si*LMNB1* (On-Target Plus SMARTpool) and siControl (D-001810) were purchased from Dharmacon. Transient transfections were performed with Dharmafect1 transfection reagent (Dharmacon) for 72 h.

Lentiviruses were produced by transient calcium phosphate transfection of 293T cells with the virus packaging plasmids, p8.91 and pVSVg, as well as with the lentiviral expression vector that contained the sequence of interest. Titration was performed approximately 10 days after infection using puromycin (1 μg/ml) to select clones. The pLKO-shp21^{CIP1} (shp21:CCGGCCGCGACTGTGATGCGCTAATC TCGAGATTAGCGCATCACAGTCGCGGTTTTTG) was purchased from Sigma. The efficiency of each shRNA and siRNA was checked routinely by RT-qPCR or western blotting.

Real-time qPCR

qPCR was used to determine the efficiency of siRNA down-regulation and for ChIP validation. For siRNA inhibition, total RNA (RNeasy Mini Kit, Qiagen) was reverse transcribed using the High-Capacity RNA-to-cDNA kit (Thermo Scientific). qPCR was performed using an Applied StepOnePlus system (Life Technologies) with SYBR green master mix (Roche, 4913914 001). Only siRNA transfections giving rise to a reduction of ≥75% were used in this study.

Immunofluorescence-FISH

Cells were grown on glass coverslips at about 70–80% confluency and fixed in 3.7% formaldehyde. Immunofluorescence coupled with FISH was performed as previously described (21).

To perform immunofluorescence-FISH in paraffin-embedded tissue sections, the samples were incubated twice with xylene for 5 min, followed by washes in progressively decreasing concentrations of ethanol (100%, 90%, 70% and 40%) for 5 min each, and then washed in 1X PBS for another 5 min. Next, antigen unmasking was carried out in 10 mM sodium citrate, 0.05% Tween-20 pH 6 solution for 45 min at 95°C. The sections were dehydrated in 95% ethanol for 3 min and air-dried follow by PNA hybridization.

Image acquisition and analysis

Images were acquired with a Zeiss LSM-888 inverted confocal laser scanning microscope. A minimum of 18 z-planes were acquired with a 63× oil immersion objective (Plan-Apochromat 63×/1.4 Oil DIC). Images were analyzed with the ZEN 2009 (Zeiss).

Western blotting

Total protein extracts were obtained using ice-cold RIPA buffer for 30 min. Samples were separated by SDS-PAGE electrophoresis using NuPAGE Mini gels (Life Technologies). Proteins were transferred onto Protran BA 85 nitrocellulose membranes (Whatman, GE Healthcare) followed by at least 1 h blocking with PBST in 5% skim milk. Hybridization with primary antibodies was performed overnight at 4°C followed by 1 h incubation with secondary horseradish peroxidase-conjugated antibodies. Membranes were developed using the Luminata Forte HRP substrate (Millipore) and exposed in the Fusion Solo apparatus (Vilbert Lourmat).

Native chromatin immunoprecipitation

Native ChIP was performed as described in Rai and Adams (14) with some modifications. Briefly, cells were grown at about 70% confluency, scraped in cold PBS to detach them and resuspended in MLB:H_2O 1:4 buffer (MLB; 50 mM Tris pH 7.5; 150 mM NaCl; 0.5% NP40 and 15 mM $MgCl_2$) supplemented with proteinase inhibitors. The mix was immediately transferred to Eppendorf tubes and kept on ice for 10 min and centrifuged for 3 min at 300 × g at 4°C. The supernatant was removed, and the pellet was resuspended in 400 μl of BB buffer (50 mM Tris pH 7.5; 300 mM NaCl; 0.5% NP40 and 2.5 mM $MgCl_2$) with proteinase inhibitors and 120 U of Benzonase (Sigma, E1014). The solution was incubated on ice for 30 min and 40 μl were taken for DNA quantification followed by a short centrifugation step of 3 min at 300 × g at 4°C. The supernatant was transferred to a clean Eppendorf tube containing an equal volume of DB solution (50 mM Tris pH 7.5; 300 mM NaCl; 0.5% NP40 and 15 mM EDTA) with proteinase inhibitors. Next, 150 μl of magnetic beads (Dynabeads, Life Technologies) with the desired antibody were added to the mix for 6 h at 4°C. Previously, the magnetic beads were washed 3 times with 1X PBS and 0.5% bovine serum albumin followed by the addition of 5 μg of the desired antibody.

Next, the mix containing the immunoprecipitated chromatin was washed 3x with a solution containing 50 mM Tris pH 7.5; 150 mM NaCl; 0.5% NP40 and 5 mM EDTA, followed by three washes of a solution containing 50 mM Tris pH 7.5; 300 mM NaCl; 0.5% NP40 and 5 mM EDTA. Finally, the beads were recovered, and the chromatin was eluted with a 1% SDS, 0.1 M $NaHCO_3$ solution. The solution was treated with RNase (10 mg/ml for 20 min), proteinase K (10 mg/ml for 1 h at 50°C) followed by phenol–chloroform purification and ethanol precipitation. Quantification of immunoprecipitated DNA was performed with the Qubit HS kit (Thermo Scientific).

Slot blotting

The DNA obtained from native ChIP experiments was denatured (0.5 M NaOH, 2 M NaCl and 25 mM EDTA) and blotted onto nylon membranes using a slot blot apparatus, crosslinked and hybridized with radioactively labeled probes. The membranes were exposed to phosphor imager screens and the signal intensity was quantified with ImageQuant software.

ChIP-sequencing and analysis

γH2AX ChIP-seq library preparation was performed using the MicroPlex Library Preparation kit v2 (Diagenode, C05010012) while single-end sequencing (read length: 75 bp) was performed using the Illumina Nextseq 500/550 High output v2.5 system according to the manufacturer's instructions. Two biological replicates per condition were performed (∼45–60 million reads per sample). Reads were trimmed and cleaned using fastP software (15) and deduplicated using Clumpify software from the BBmap package (available at https://github.com/BioInfoTools/BBMap/blob/master/sh/clumpify.sh). Reads were mapped on the GRCh38 human genome assembly using Bowtie2 with default parameters (16). Broad peak calling was performed using EPIC2 program (v0.0.36) (17) with the following settings: *–genome hg38; –keep-duplicates*; *–mapq 0*. Finally, following ENCODE guidelines (18), peaks within blacklisted regions were removed. Peaks profiles were generated using the 'Score' column from EPIC2 output and bedGraphToBigWig tool from UCSC.

Motifs for different repeat elements Sat III, Sat II, telomeric, alphoid, rDNA, LINE1, Alu repeats) were searched using a homemade Python script, in raw fastq files, without considering mismatches and including reverse complement motifs. IP samples counts were normalized to their corresponding Input sample count.

RNA sequencing

Total RNA was extracted using the RNeasy mini kit (Qiagen). Paired-end sequencing (read length: 2 × 150 bp) was performed by NovoGene using an Illumina sequencer. Two biological replicates were performed for senescent cells transduced with an empty vector and three biological replicates with TRF2 expressing cells (between 30 and 50 million reads per sample). Raw RNA-seq reads were trimmed using Trimmomatic (v0.39) (19) and the minimal read length was set to 35 bp. Read mapping and genome index building were performed using STAR (v2.6.1d) (20). Reads were mapped to the human genome assembly (GRCh38) using

the -*quantMode GeneCounts* option. Differential expression analysis was performed using the DESeq2 R package (21).

Statistical analyses

GraphPad Prism 7 software was used to generate graphs and to perform statistical analysis. *P* values were obtained using either the two-tailed Student's t-test, Mann–Whitney *U* test or the Kruskal–Wallis test. Differences were considered statistically significant when $P < 0.05$ ($^{*}P < 0.01$, $^{**}P < 0.001$, $^{***}P < 0.0001$). The absence of statistical annotation indicates non-significance.

RESULTS

Pericentromeric DNA is selectively damaged during senescence

To analyze the events leading to pericentromeric heterochromatin (PCH) alterations during senescence, we cultured lung primary fibroblast MRC-5 cells under hypoxic conditions (5% oxygen) until they reached senescence and collected samples at different population doublings (PDs) (Figure 1A). We considered cellular cultures as presenescent when senescence-associated beta-galactosidase (SA-β-Gal) positive cells started to accumulate while EdU positive cells decreased and a fully senescent culture when SA-β-Gal activity was detectable in all cells and EdU incorporation accounted for <1% of the cells. As reported previously (22,23), telomeric DNA damage, as revealed by the colocalization of a telomeric peptide nucleic acid (PNA) probe with 53BP1 (TIFs- Telomere dysfunction-induced foci), gradually increases by subsequent PDs before the culture becomes fully senescent (Figure 1A). Roughly 5 PDs after the beginning of telomere uncapping, PCH DNA damage increased, as revealed by the colocalization of 53BP1 with a PNA FISH probe corresponding to Satellite III (Sat III) DNA repeats (PIFs- pericentromeric dysfunction-induced foci) (Figure 1A). Strikingly, this increase in DNA damage is not evenly distributed throughout the chromosomes since no damage was detected at the alpha-satellite (alphoid) DNA sequences, constituting the major class of centromeric DNA repeats (CIFs—centromeric dysfunction induced foci) (Supplementary Figure S1A). Thus, during replicative senescence, the accumulation of DNA damage outside telomeres appears selective for certain types of DNA repeats, e.g. pericentromeric but not centromeric repeats. To confirm and extend this finding, we performed chromatin immunoprecipitation experiments coupled to deep sequencing (ChIP-seq) with γH2AX antibodies. We analyzed highly repeated DNA sequences, largely underrepresented in the reference genome, by calculating their proportion in the ChIP-seq reads as normalized to input. This revealed a specific enrichment of reads containing Sat II, Sat III and telomere repeats, but not alphoid, rDNA and LINE-1 repeated sequences as compared to young cells (Supplementary Figure S1B), confirming and extending the analyses by microscopy of TIFs, PIFs and CIFs in young and senescent cells (Supplementary Figure S1A).

Henceforth, we set to determine the mechanism responsible for the selective damage at PCH DNA during replicative senescence.

DNA damage at pericentromeric heterochromatin precedes its decondensation at senescence onset

It was previously reported that senescence is accompanied by PCH decondensation (5,6). In our kinetic analysis of senescence, the increase in PCH DNA damage slightly precedes decondensation, as estimated by measuring the diameter of Sat III PNA fluorescent speckles (Figure 1A and Supplementary Figure S1C). As expected (6,24), PCH decondensation was accompanied by derepression of its transcription (Supplementary Figure S1D). Echoing the lack of DNA damage at centromeres, there was no detectable increase in the diameter of the centromeric foci stained by an alphoid sequence PNA probe (Supplementary Figure S1E). Instead, we observed a significant increase number of smaller centromeric foci at senescence (Supplementary Figure S1F), possibly reflecting chromatid cohesion defects (25) while Sat III foci number was barely affected (Supplementary Figure S1F). To examine whether the lack of DNA damage at centromeric regions was just the consequence of a technical constrain, we treated young MRC-5 cells (PD 28) for 24 h with bleomycin and performed CIFs using 53BP1 antibody and ChIP coupled with slot blot using a γH2AX antibody (Supplementary Figure S1G and H). Under these conditions it was possible to detect centromeric damage in both experimental settings (Supplementary Figure S1G and H), thus the absence of centromere damages during senescence cannot be merely explained by a technical difficulty to detect centromeric damages.

Next, we investigated whether the selective accumulation of PIFs and decondensation can be triggered by other senescence-inducing stressors. After four days of bleomycin treatment, the fully senescent culture exhibits a dramatic increase in global DNA damage, which is attenuated after ten days of bleomycin removal (Supplementary Figure S1I). However, telomeric, as expected (26,27), and PCH DNA damage persist, showing that, in senescent cells, both regions are sites of irreparable damage (Figure 1B). In hand with PCH DNA damages, PCH decondensation started 4 days after bleomycin treatment (Figure 1C). Centromere damage, on the other hand, remained low (Figure 1B).

The accumulation of damaged and decondensed PCH appears as a general hallmark of cellular senescence and organismal aging since we observed it in senescent cells of two other human diploid fibroblast cell lines, WI-38 and IMR-90 (Supplementary Figure S2A and B) as well as in mesenchymal stem cells (MSC) from old individuals and human dermal fibroblasts (Supplementary Figure S2C–F). In aging MSC, there is also an increase of DNA damage at telomeres but not at centromeres (Supplementary Figure S2A and C), indicating that the selectivity of PCH and telomere damage observed in senescent fibroblasts in culture it is also true during natural MSC aging.

Selective pericentromeric heterochromatin dismantling occurring at senescence onset

We further characterized the PCH alterations occurring at the senescence onset. To detect DNA double-strand breaks (DSBs) at PCH, we used neutral comet assays coupled with specific PNA FISH probes. Compared to young cells, senescent cells had longer comet tails enriched in telomeric DNA

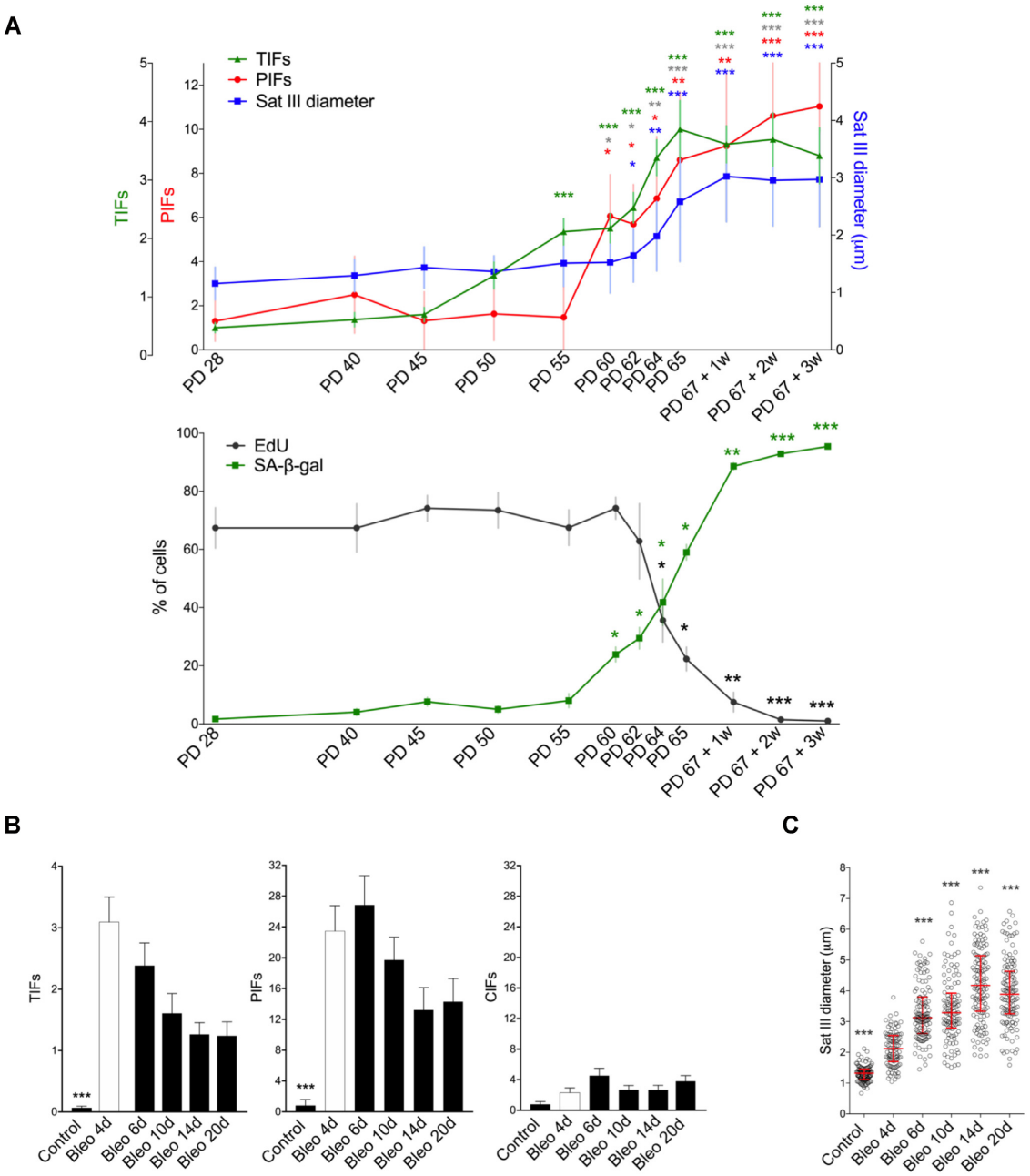

Figure 1. Pericentromeric damage during cellular senescence**.** (**A**) MRC-5 cells collected at different population doublings (PDs) until senescence. Top panel, telomeric damage (TIFs), pericentromeric damage (PIFs) and opening of Sat III (represented as the diameter of the Sat III PNA signal in μm) were estimated from immunofluorescent confocal microscopy images by the colocalization of 53BP1 antibody and a PNA probe with the corresponding repeat element. TIFs represent the number of colocalizations per nucleus, while PIFs show the percentage of PNA signal colocalizing with 53BP1. The bottom panel shows the percentage of cells incorporating EdU (1 μM for 24 h) and the percentage of cells positive for senescence-associated β-galactosidase. Data represent the mean ± SD of three biological replicates. Statistical analyses were performed using the Kruskal–Wallis test ($^{*}P < 0.01$; $^{**}P < 0.001$; $^{***}P < 0.0001$). (**B**) Young MRC-5 PD 28 were treated with 10 μg/ml bleomycin for 4 days. Fresh media without bleomycin was added to the culture and kept for further 20 days. TIFs, PIFs and CIFs and (**C**) Sat III opening quantification. The mean ± SD of three biological replicates is shown. Statistical analyses were performed using the Kruskal–Wallis test ($^{***}P < 0.0001$).

and Sat III, but not in alphoid DNA sequences (Figure 2A). Thus, the DNA damage response (DDR) activation at PCH in senescent cells is likely to result from DSB formation. Then, we asked whether this high rate of DSBs led to illegitimate recombination events between pericentromeric DNA repeats by using chromatin-orientation FISH (CO-FISH) (13). We found that the percentage of chromosomes with recombination events at PCH DNA increased in pre-senescent as compared to young cells (Figure 2B). This result also indicates that PCH alterations are detectable in dividing pre-senescent cells and thus is not an event specifically occurring when the cells stop dividing in the senescent state.

The high level of PCH DSBs and recombination events during senescence could result in gains or losses of DNA sequences. Thus, we measured PCH DNA length by a pulse-field gel electrophoresis assay followed by Southern blotting of the resolved genomic DNA cut with the HindIII restriction enzyme. This restriction cutting releases PCH DNA fragments of around 200 kb, which were specifically hybridized with Sat II and Sat III probes. This restriction size decreased by roughly 50 kb in senescent cells (Figure 2C) and start occurring in pre-senescent cells (Supplementary Figure S2G), around the same time as the relaxation of Sat III repeats (Figure 1A). Such a DNA repeat shortening also occurs, as expected, for telomeric DNA (Supplementary Figure S2H) but not for other repetitive elements such as Alu, rDNA, alphoid DNA or microsatellites (Figure 2C and Supplementary Figure S2I). Concomitantly, by combining DAPI and satellite III PNA staining, we observed a progressive increase in the number of cytosolic DNA specifically enriched in satellite III sequences during senescence establishment (Figure 2D).

Overall, these results show that the PCH is profoundly dismantled during senescence combining DNA damage and breaks, decondensation, transcriptional derepression, illegitimate inter-chromatid recombination, DNA loss and cytosolic DNA accumulation. The selectivity of this phenotype to PCH is shown by the absence of this combination of senescence-associated events at other highly repeated regions of the human genome, such as rDNA, LINE-1 and alphoid satellite repeats.

Pericentric dismantling coincides with TRF2 decrease in pre-senescent cultures

To examine the sequence of events linking telomere shortening to PCH dismantling, we measured the expression of the six shelterin subunits in the same samples as those used in the time points leading to the establishment of the senescent state (Figure 3A and Supplementary Figure S3A). Only TRF2 and TPP1 were progressively downregulated to roughly 50% of their initial level. Impressively, the appearance of PIFs precisely correlates with the reduction in TRF2 and TPP1 expression (Figure 3A). Since TRF2 is known to bind PCH DNA and protect it against damage (22), we asked whether this is also true for TPP1. As expected, inhibition of TRF2 and TPP1 in young cells increased the frequency of TIFs, however, only TRF2 depletion leads to a specific increase of PCH DNA damage (Figure 3B and Supplementary Figure S3B, C), making unlikely a direct role of TPP1 in senescence-associated PCH instability.

Then, we examined whether the lower levels of TRF2 in senescent cells have an impact on its association with PCH DNA. As quantified by ChIP, the TRF2 binding to PCH DNA was almost entirely lost in senescent cells, predicting an important impact of the senescence-associated TRF2 downregulation on PCH stability (Figure 3C). In contrast, approximately 50% of TRF2 remained bound to telomeres. Parallel ChIP experiments made with γH2AX antibodies show, as expected, an increase in DNA damage at both telomeres and PCH (Figure 3C).

Overall, these results suggest that PCH integrity is specifically altered during replicative senescence establishment as a consequence of TRF2 downregulation.

TRF2 decrease is sufficient to drive pericentromeric dismantling

Next, we asked whether TRF2 downregulation was sufficient to recapitulate the PHC dismantling phenotype observed at the onset of senescence. A 3-day downregulation of *TERF2* expression in young MRC5 cells specifically triggers the formation of DNA damage (Figure 3B), DSBs and decondensation at PCH (Supplementary Figure S3D and S3E). Then, we used a HeLa cell line containing an sh*TERF2*-inducible doxycycline system (28). After 7 and 9 days of TRF2 inhibition, PCH decondensed (Figure 3D) and the length of the PCH DNA HindIII fragments progressively decreased by roughly 50 kb (Figure 3E), while PCH DNA became more recombinogenic as revealed by CO-FISH (Figure 3F) and the number of cytosolic DNA increased (Figure 3G). The cytosolic DNA is composed primarily of telomeric sequences and PCH DNA while centromeric repeats were barely detected (Figure 3G), highlighting again the specificity of the effect of TRF2 downregulation on PCH dismantling.

TP53 activation leads to DNA damage specifically at pericentromeric DNA

Since degradation of TRF2 in pre-senescent cells was previously shown to be mediated by TP53-dependent Siah1 upregulation (29), we asked whether TP53 is involved in PCH dismantling. As expected, inhibition of TP53 expression counteracted the downregulation of TRF2 in pre-senescent cells (Figure 4A). Noteworthy, there is no apparent increase in TP53 protein level when the cells enter into senescence (Figure 4A), in agreement with a previous report showing that, in replicative senescent fibroblasts, p53 is activated by post-translational modifications and not by protein stabilization (30). Impressively, even though total DDR activation increased upon TP53 depletion (Figure 4B), PCH DNA damage significantly decreased in pre-senescent (PD 60) and senescent cells (PD 67) as compared to control cells, while the levels of telomere damage remained unchanged (Figure 4C). Even though the amount of cytosolic DNA significantly increases after TP53 knockdown, cytosolic DNA containing PCH was less abundant, reducing from 60% in siControl cells to 30% in siTP53 (Figure 4D) and PCH opening was also prevented upon TP53 depletion (Figure

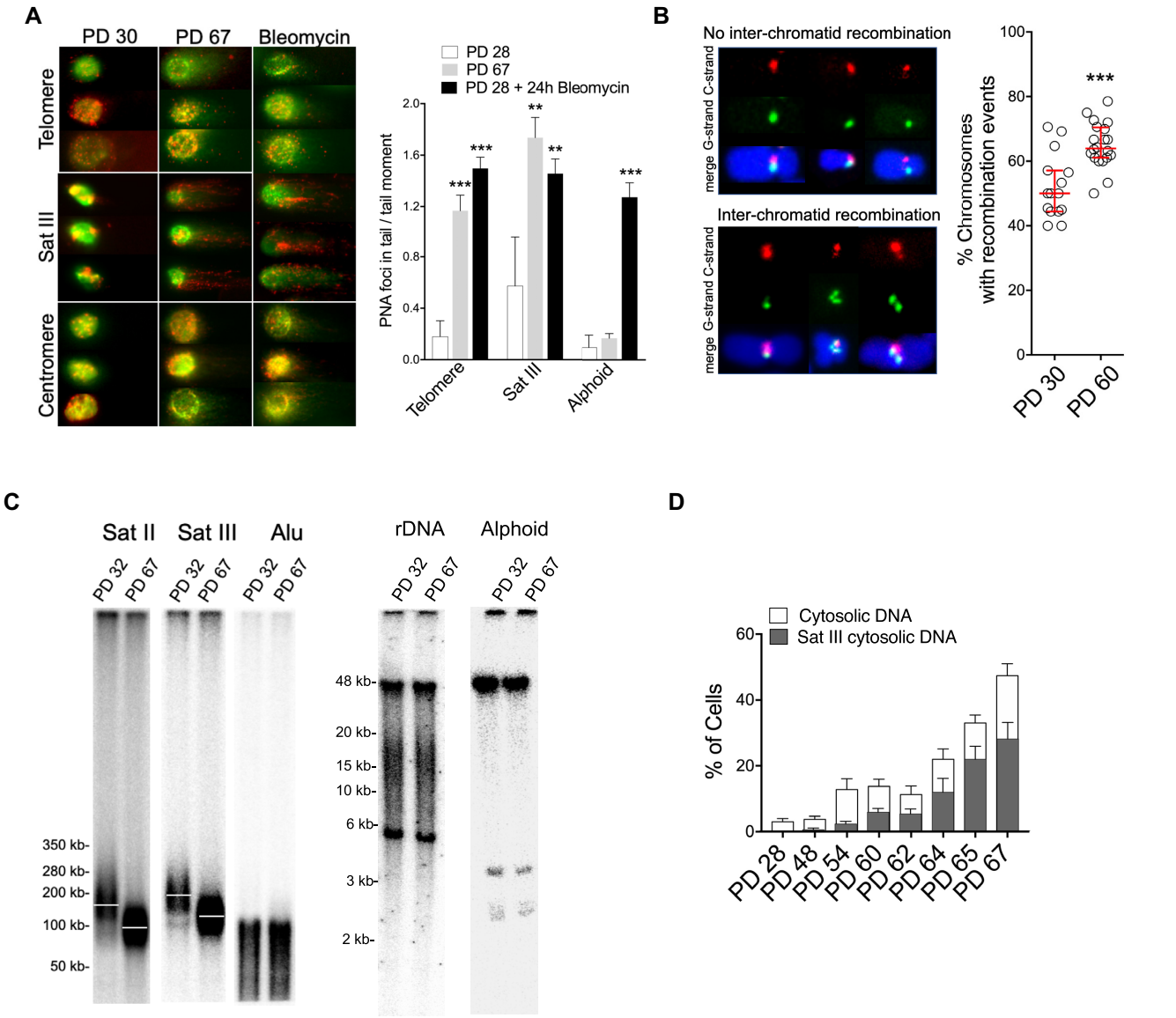

Figure 2. Selective pericentromeric DNA instability at senescence onset. (**A**) Neutral comet assay. Bleomycin treatment (50 μg/ml for 24 h) of young MRC-5 cells (PD 28) was used as a positive control for double-strand breaks. Graphs show the number of PNA foci in the tail of the comet divided by the tail moment (tail length × DNA signal in the tail / total DNA signal). DNA is shown in green (YOYO-1), whereas the PNA probe signal is in red. Error bars represent SEMs of at least 60 cells. Statistical analyses were performed using the Kruskal–Wallis test ($^{**}P < 0.001$; $^{***}P < 0.0001$). (**B**) Pericentromeric instability assessed by CO-FISH in young (PD 28) and pre-senescent (PD 60) MRC-5 cultures. Quantification was performed by calculating the percentage of chromosomes containing a pattern of staining different from a single-side PNA signal. This does not discriminate between stable inversion events present in those regions. Error bars ± SD of at least 15 metaphases. Mann–Whitney *U*-test ($^{***}P < 0.0001$) was used for statistical analysis. (**C**) Southern blots showing the distribution of MRC-5 Sat II, Sat III and Alu repeats at different PDs following digestion with HindIII. DNA was digested with BamHI to assess for rDNA and alphoid repeat size distribution. The separation of DNA fragments was carried out using a pulsed-field gel electrophoresis system. (**D**) Percentage of cells with cytosolic DNA stained with a Sat III PNA probe. Error bars show the SD of three biological replicates.

4E). These results show that TP53 leads to DNA damages, decondensation and loss selectively at PCH.

In addition, in MRC-5 cells exposed to bleomycin for 4 days, there was also a correlation between the increased TP53 expression and gradual reduction of TRF2 levels (Supplementary Figure S4A), while depletion of p53 restored the levels of TRF2 (Figure 4F). In agreement with this result, treating young MRC5 cells with the MDM2-p53 interaction inhibitor, Nutlin-3a, led to TRF2 loss with an augmentation of PCH DNA damage and decondensation (Supplementary Figure S4B-D). Therefore, the TP53-dependent control of TRF2 expression and PCH instability is not limited to cells experiencing telomere shortening.

TRF2 downregulation is necessary to drive pericentromeric dismantling at senescence onset

Next, we asked whether the TP53-dependent TRF2 downregulation is necessary for the senescence-associated PCH dismantling phenotype. To this end, we ectopically expressed TRF2 from PD 50 until senescence, to counteract its TP53-dependent degradation (Figure 5A). As negative

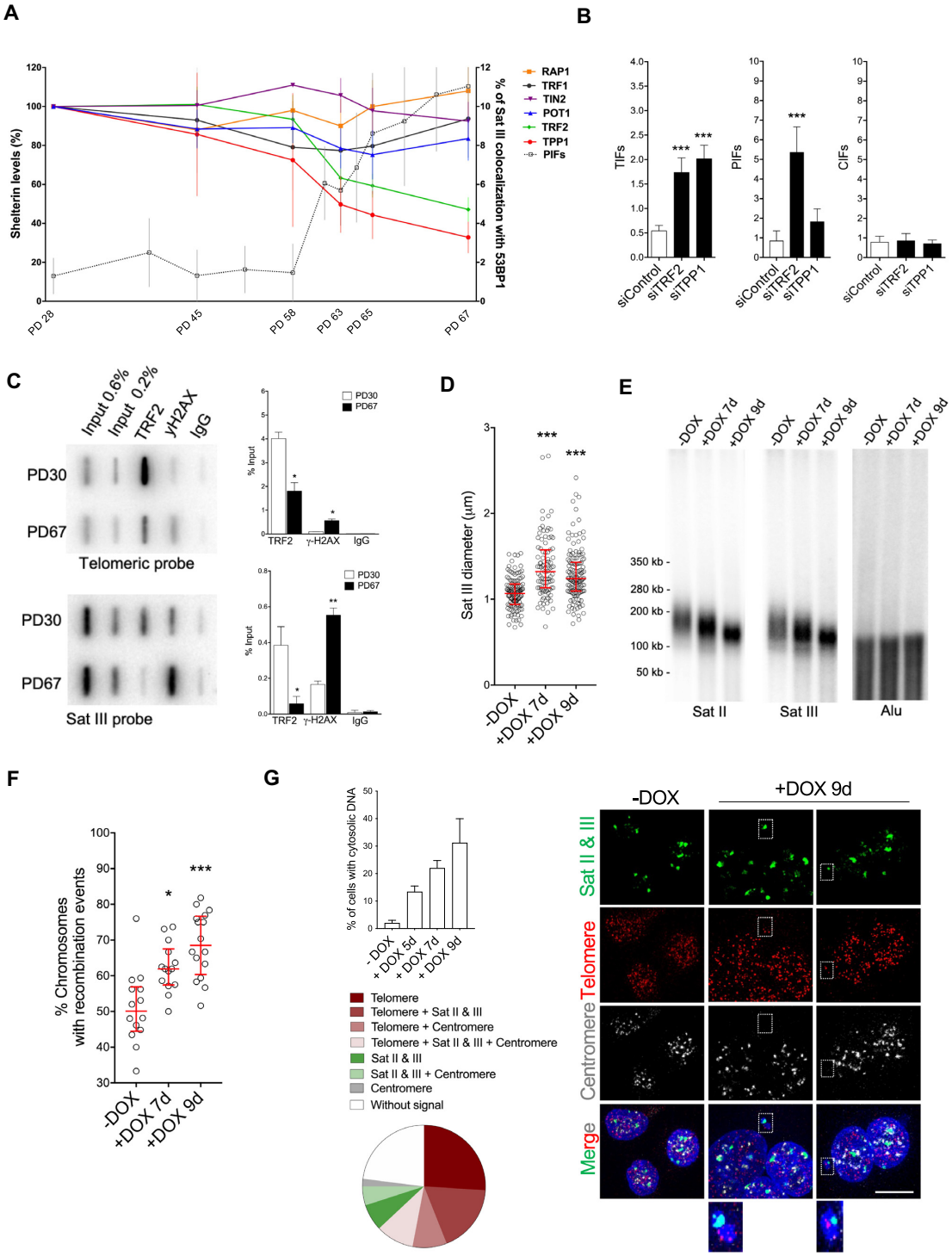

Figure 3. TRF2 protects against PCH damage. (**A**) Expression of shelterin proteins at different population doublings in MRC-5 based on western blotting of two biological replicates. PIFs are indicated with a dotted line. (**B**) TIFs, PIFs and CIFs of young (PD 28) MRC-5 cells treated for three days with the indicated siRNA. PIFs were measured by combining Sat II and Sat III PNA probes. Data represent the mean ± SD of three biological replicates. Statistical analyses were performed using the Kruskal–Wallis test ($^{***}P < 0.0001$). (**C**) Native ChIP of young (PD 30) and senescent (PD 67) MRC-5 cells. The immunoprecipitated DNA obtained with TRF2 and γH2AX antibodies and IgG control was spotted onto slot blots and hybridized with either a telomeric or a Sat III radioactively labeled probe. Quantification shows the enrichment as a percentage of input from three independent experiments. Statistical analysis was performed using an unpaired two-tailed t-test. Error bars represent mean ± SD; $^{*}P < 0.01$, $^{**}P < 0.001$. (**D**) Sat III opening, (**E**) Sat II, Sat III and Alu length distribution, and (**F**) Sat III inter-chromatid recombination events of HeLa cells treated with doxycycline (DOX) to deplete TRF2 expression at a final concentration of 1 μg/ml. (**G**) Percentage of cytosolic DNA (top left panel) upon different TRF2 knockdown times. Cells were co-stained with different PNA probes targeting telomeres, centromeres and pericentromeres (right panel). The distribution of PNA cytosolic staining was similar amongst the different time points. The distribution at 9 days of TRF2 knockdown (+DOX 9d) is shown (left bottom panel). Data represent the mean ± SD of three biological replicates. Statistical analyses were performed using the Kruskal–Wallis test ($^{*}P < 0.01$; $^{***}P < 0.0001$).

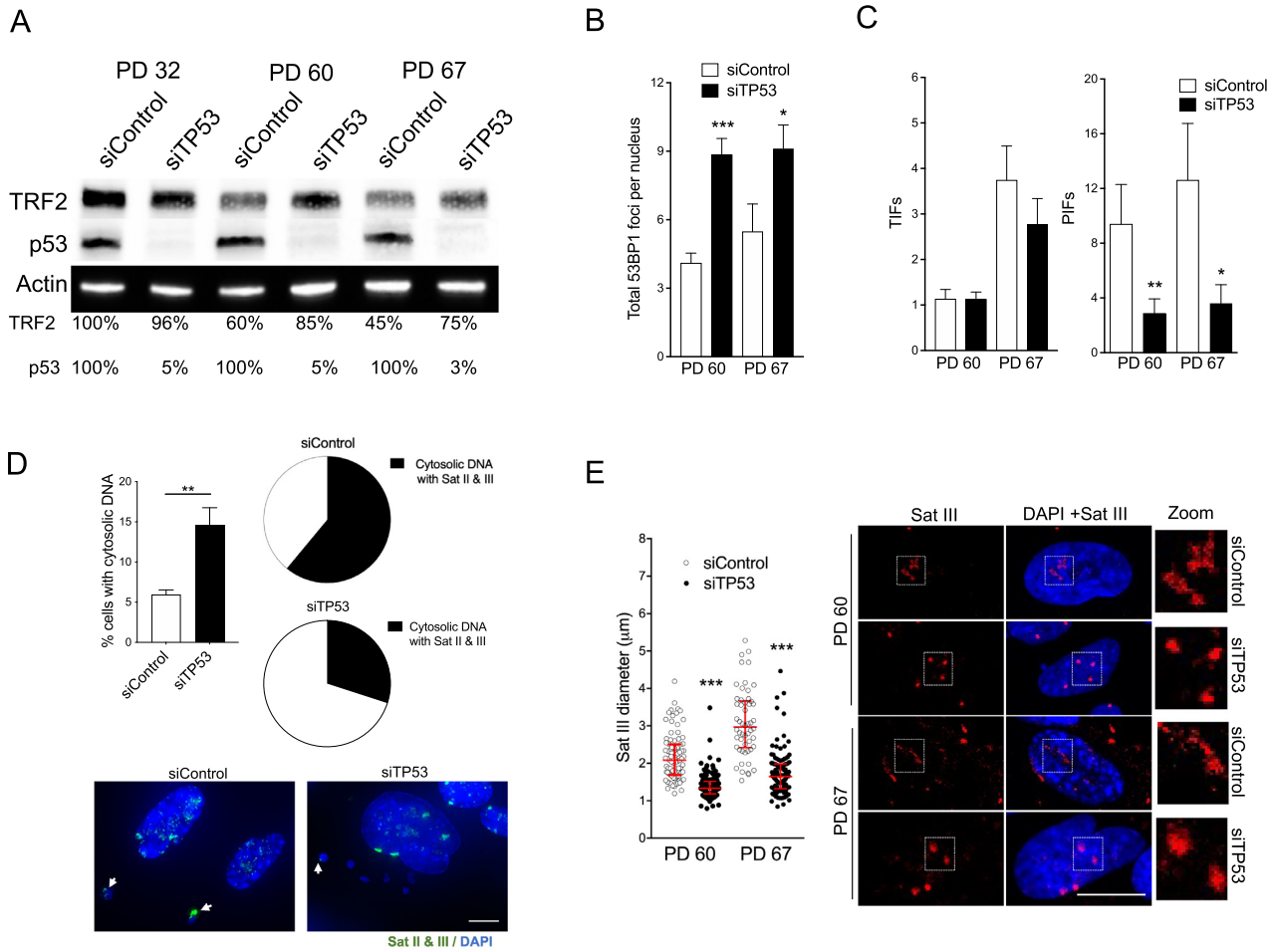

Figure 4. TP53-dependent TRF2 downregulation. (**A**) Immunoblotting showing the expression of TRF2 and p53 in young MRC-5 (PD 28) after three days of p53 knockdown. (**B**) Immunofluorescence detection of total 53BP1 spots per nucleus, (**C**) mean number of TIFs, PIFs of young MRC-5 cells ($^{*}P < 0.01$; $^{**}P < 0.001$; $^{***}P < 0.0001$; Mann–Whitney *U*-test). (**D**) The percentage of cells displaying cytosolic DNA and the proportion of them containing Sat II and III are shown. (**E**) Sat III opening of pre-senescent (PD 60) and senescent (PD 67) cells. Data represent the mean ± SD of three biological replicates. Statistical analyses were performed using the Mann–Whitney *U*-test ($^{*}P < 0.01$; $^{**}P < 0.001$; $^{***}P < 0.0001$). (**F**) Western blotting showing the expression of p53 and TRF2 in young (PD 28) MRC-5 cells treated with 10 μg/ml bleomycin for 4 days. Fresh media without bleomycin was added to the culture and kept for further 20 days. Three days before collecting the cells siRNA was performed, $n = 1$.

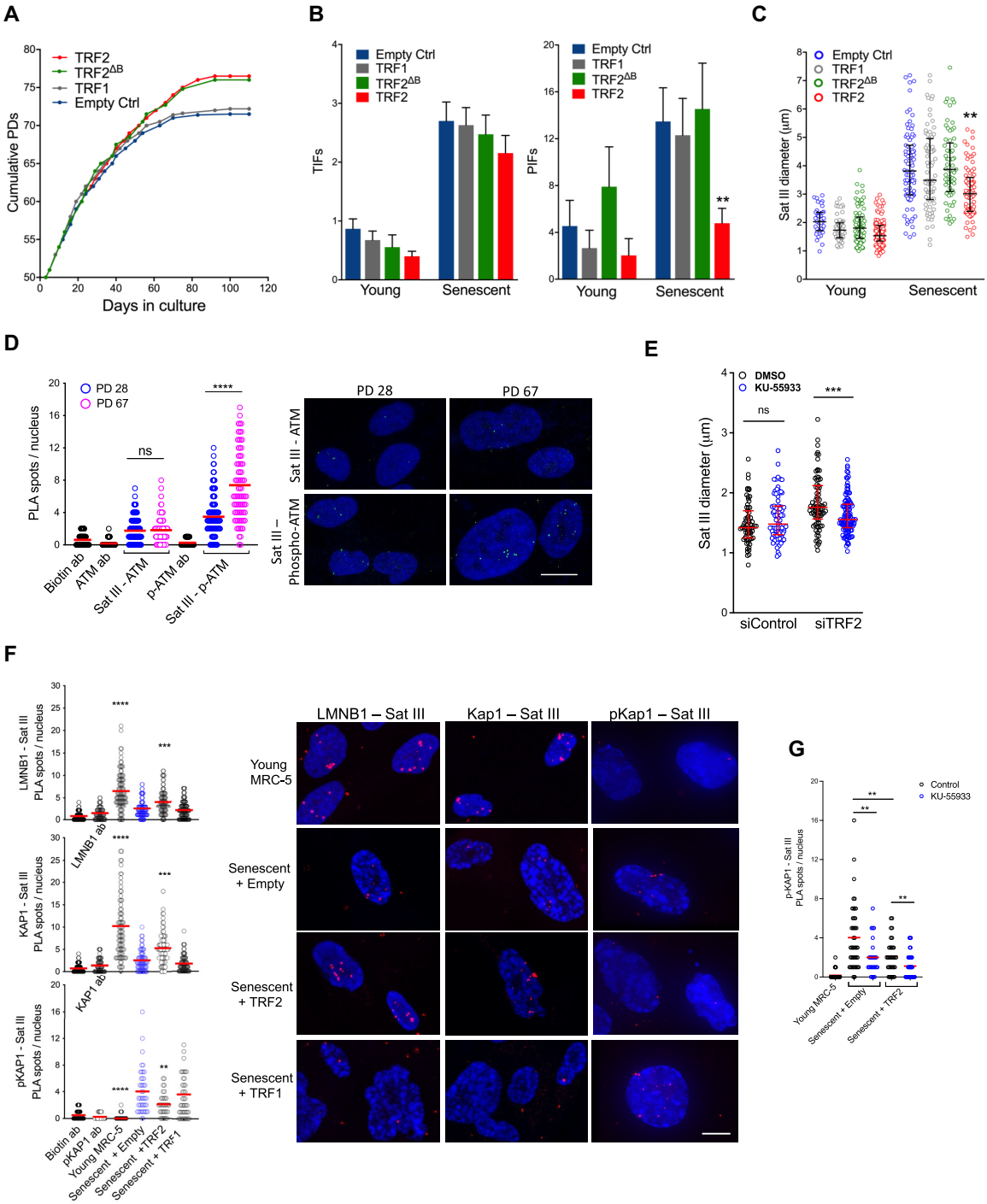

Figure 5. TRF2 is necessary to maintain PCH stability during replicative senescence. (**A**) Growth curve of MRC-5 cells transduced at PD 50 with lentivirus containing an empty vector, TRF1, the full-length TRF2 or the truncation TRF2ΔB form. Cells entered into senescence at PD 71 for control and TRF1 transduced cells and at PD 75 for TRF2 and TRF2ΔB cells. The cells were allowed to grow until senescence at 5% oxygen. (**B**) TIFs, PIFs and (**C**) Sat III opening of young MRC-5 cells (PD 28) transduced for 6 days with at a lentivirus containing an empty vector or the full-length TRF2. Pre-senescent cells (PD 50) were transduced with empty or TRF2 expressing lentivirus and grow until they senescence (PD 71 for empty control and PD 75 for TRF2 expressing cells) at 5% oxygen. Data represent the mean ± SD of three biological replicates. Statistical analyses were performed using the Kruskal–Wallis test ($^{*}P < 0.01$; $^{**}P < 0.001$; $^{***}P < 0.0001$). (**D**) Proximity Ligation Assay (PLA) using an ATM or a phospho-ATM antibody together with a biotin antibody with recognizes Sat III PNA probes already conjugated to biotin. Data shows the mean ± SD of three biological replicates. Statistical analyses were performed using the Kruskal–Wallis test ($^{****}P < 0.00001$). (**E**) Sat III opening in MRC-5 young cells (PD 28) with TRF2 knockdown for 72 h and treated with 10 μM of the ATM inhibitor KU-55933 24 h before harvesting. Data represent the mean ± SD of three biological replicates. Statistical analyses were performed using the Kruskal–Wallis test ($^{*}P < 0.01$; $^{***}P < 0.0001$). Bar = 10 μM. (**F**) PLA using either LaminB1, Kap1 or phopho-KAP1 antibody together with a biotin antibody binding a Sat III PNA probe. Approximately 80 nuclei were analyzed per condition. Statistical analyses were performed using the Kruskal–Wallis test ($^{***}P < 0.0001$). (**G**) PLA on Sat III and phospho-KAP1 of senescent cells expressing an empty or a TRF2 expressing vector. Twenty-four hours before harvesting, the ATM inhibitor KU-55933 at 10 μM was used.

controls, we ectopically expressed TRF1, which is not required for PCH stability, and TRF2$^{\Delta B}$, a separation of function form of TRF2 preserving its telomere capping properties but unable to protect PCH (31). Cells that ectopically expressed TRF2 and TRF2$^{\Delta B}$, but not TRF1, bypassed the proliferative capacity of the control culture, and lengthened it by approximately 5 PDs before entry into a second senescent state (Figure 5A). These results are in agreement with a previous work showing that TRF2 overexpression delays senescence (32). The second senescence arrest of MRC-5 cells overexpressing TRF2 corresponds to p16^{CDKN4a} activation in contrast to replicative senescent cells mostly inducing p21^{WAF1} (Supplementary Figure S5A). Importantly, ectopic expression of TRF2, but neither of TRF1 nor TRF2$^{\Delta B}$, prevents PCH DNA damage and PCH decondensation (Figure 5B and C). Moreover, the PCH DNA length is partially restored by the ectopic expression of TRF2 during senescence (Supplementary Figure S5B). The low amount of centromeric DNA damage at senescence is not affected by TRF2 dosage (Supplementary Figure S5C), illustrating again the PCH-specificity of the TRF2 role at senescence. These results also reveal that PCH dismantling does not trigger replicative senescence arrest since TRF2$^{\Delta B}$ ectopic expression does not rescue PCH stability but bypasses senescence as TRF2. Unexpectedly, ectopic expression of TRF2 or TRF2$^{\Delta B}$ did not restore telomere protection (Supplementary Figure S5D); a result that cannot be explained by a telomere DNA lengthening effect.

The fact that TRF2 is required for normal PCH replication (31,33) and that PCH DNA damage appears in dividing presenescent cells when the levels of TRF2 decline suggest that PCH replication defects are triggered by the decrease in TRF2 level. We addressed this point by assaying for PCH replication in presenescent cells. To this end, we used a PLA approach to monitor the proximity of PCNA to a Sat III PNA probe (Supplementary Figure S5E). We found a high level of association in young MRC-5 cells which is significantly reduced in presenescent cells and partially prevented by restoring a high level of TRF2 expression (Supplementary Figure S5E). We noticed a low number of spots outside the nucleus (one per nucleus on average) across all experimental conditions, suggesting an unspecific signal in the PLA experiment. Importantly TRF2 does not affect centromeric DNA replication (Supplementary Figure S5E). These results show that the presenescent decline of TRF2 indeed triggers replicative defects at PCH. However, since TRF2 level restoration fully rescued PCH damage but only partially the PCH replication defects, suggests that the presenescent decline of TRF2 is also responsible for replication-independent PCH damages. This hypothesis was tested by restoring TRF2 levels in bleomycin-induced arrested cells. This led to a decrease in PCH DNA damage and decondensation (Supplementary Figure S5F and S5G) while telomere, centromere and overall cell damage remained unchanged (Supplementary Figure S5H), showing that TRF2 can specifically control PCH structure independently of replication. We conclude that the decline in TRF2 level triggered by different senescence inducers leads to PCH damages through its function in PCH replication, as revealed in dividing presenescent cells, and by replication-independent mechanisms, as revealed in bleomycin-arrested cells.

Overall, these results show that the TP53-dependent TRF2 decline occurring during replicative senescence or upon genotoxic stress is responsible for the specific PCH dismantling phenotype.

The ATM DNA damage response triggered by TRF2 downregulation leads to pericentromeric decondensation

Next, we envisaged the possibility that TRF2 downregulation triggers PCH decondensation through ATM activation. First, we set to investigate the activation of ATM during replicative senescence at PCH. For that, we used a PLA approach and we could not find any difference between the interaction of Sat III DNA and ATM in young vs senescent cells (Figure 5D), however phospho-ATM significantly increased (Figure 5D), showing that ATM is activated at PCH in senescent cells. The pharmacological inhibition of ATM (KU-55933) restored PCH decondensation in senescent cells (Supplementary Figure S6A) and prevented PCH decondensation in MRC-5 and HeLa TRF2-compromised cells (Figure 5E and Supplementary Figure S6B) showing that ATM activation is required for the PCH decondensation upon TRF2 downregulation. The fact that the quantity of H3K9me3 at PCH was not altered either by TRF2 loss or overexpression (Supplementary Figure S6C and D) shows that the effect of TRF2 loss and ATM activation on heterochromatin structure is not acting at the level of this key histone mark of heterochromatin but rather at a higher-order structural level. Thus, we examined the hypothesis that the association of two key heterochromatin factors, KRAB-associated protein 1 (KAP1) and Lamin B1 (LMNB1) (5,34,35), to PCH is controlled by TRF2 and ATM at the onset of senescence since they are downregulated during senescence (8,12). We show that the loss of KAP1 or LMNB1 in young MRC5 cells leads to PCH decondensation in an ATM-dependent manner and also leads to loss of PCH signal (Supplementary Figure S6E and F). Inhibition of both KAP1 and LMNB1 at the same time resulted in no additive effect suggesting both proteins act in the same pathway (Supplementary Figure S6E). Notably, the senescence-coupled reduction of KAP1 and LMNB1 localization at PCH was reversed by the ectopic expression of TRF2 (Figure 5F and Supplementary Figure S6G, H). Importantly, while the association of KAP1 to Sat III DNA increase upon TRF2 expression, the levels of phospho-KAP1 decreased (Figure 5F), and the inhibition of ATM is enough to decrease the signal of phospho-KAP1 in either control or TRF2 expressing senescent cells (Figure 5G). We conclude that the ATM activation triggered by TRF2 loss during senescence controls the release of KAP1 and LMNB1 from PCH and its subsequent decondensation.

Pericentromeric heterochromatin dismantling triggers an interferon response

The cytosolic PCH DNA is selectively stained with the immune sensor cyclin GMP-AMP synthase (cGAS) (Figure 6A), in agreement with a previous report showing that cGAS preferentially binds Sat III DNA (36). This, along

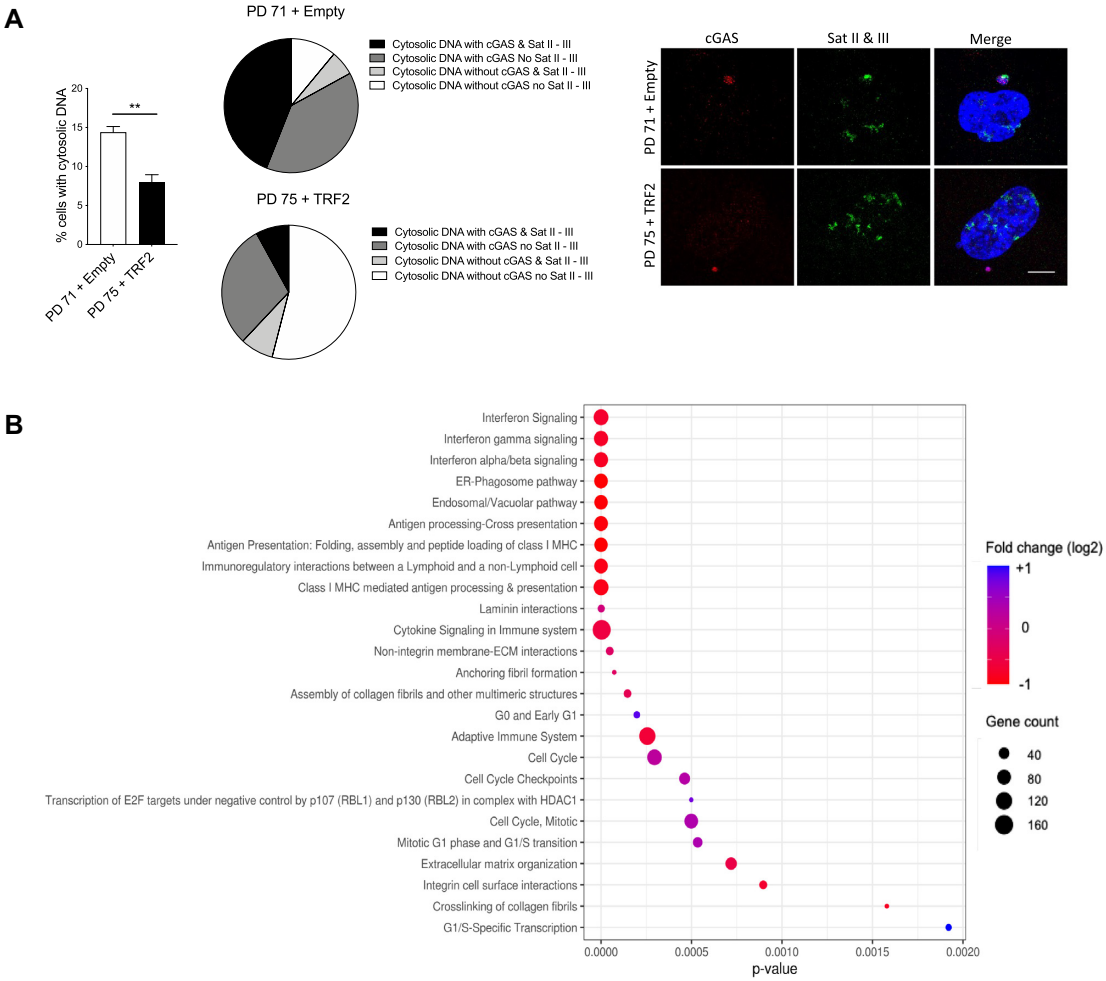

Figure 6. TRF2 prevents cGAS activation by preventing the release of PCH DNA. (**A**) The percentage of MRC-5 senescent cells transduced with TRF2-expressing lentivirus or control containing at least one cytosolic DNA signal is shown. Data represent the mean ± SD of three biological replicates (left panel). Pie charts show the proportion of cytosolic DNA staining with cGAS and/or satellite repeats (middle panel). Representative confocal images of cells stained with cGAS (red) and a combination of Sat II & III PNA probes (green) are displayed (right panel). (**B**) Reactome pathway analysis of RNA-seq differential expression data of senescent cells with and without ectopic expression of TRF2.

the fact that the ectopic expression of TRF2 in senescent cells reduced the proportion of cytosolic PCH DNA (Figure 6A), suggests a contribution of the TP53–TRF2–PCH axis to the pro-inflammatory properties of senescent cells. To test this hypothesis, we asked whether an immunological transcriptional signature depends upon TRF2 expression levels. The transcriptome of senescent cells with a restored level of TRF2 shows, as compared to control senescent cells, revealed an underrepresentation in pathways related to the immune system such as the interferon-alpha/beta signaling pathway and an overrepresentation in cell-cycle pathways (Figure 6B). Notably, the expression of five prominent interferon-stimulated genes, IFIT2, IFIT3, OASL, TRIM25 and ISG15, is downregulated upon TRF2 overexpression. Finally, we measured the expression of the five interferon-stimulated genes after TRF2 inhibition in a non-senescence system in HeLa cells, where TRF2 depletion is enough to increase cytosolic DNA containing satellite II and III (see Figure 3G). In agreement with the senescence situation, IFIT2, IFIT3, OASL and ISG15 significant increase after seven days of TRF2 inhibition (Supplementary Figure S7).

Overall, we conclude that the programmed TP53-dependent TRF2 decrease during senescence triggers a selective PHC dismantling process that increases the amount of cytosolic cGAS-associated PCH DNA and activates an interferon response.

Senescence-associated pericentromeric heterochromatin dismantling as a mechanism of chromosome rearrangement in cancer cells

Since cancer cells can derive from senescent cells that escaped cell cycle checkpoints (37), we asked whether the senescence-associated PCH dismantling could promote the aberrant chromosome rearrangements involving heterochromatin that are observed in numerous cancer cells (38–41). Thus, we used a model of senescence escape by transducing fully replicative senescent cells with a shp21^{CIP1}-expressing lentivirus (42). Senescent cells began to divide

seven days post-infection (DPI) with shp21^{CIP1}, the cultures were expanding homogeneously with no indication of clonal growth (Figure 7A). We co-transduced post-senescent shp21^{CIP1} cells with TRF2, hTERT or an empty lentivirus vector (Figure 7A). Cells expressing an empty vector entered back into senescence after 9 PDs in culture, while the cells expressing the full-length TRF2 continued to divide ∼12.5 PDs after viral infection. While the global DDR remained nearly constant (Figure 7B), the number of PCH DNA damages markedly decreased in post-senescent cells overexpressing TRF2 at 10 DPI (Figure 7C), but the levels of TIFs remained high reflecting the continuous telomere shortening in these cells (Figure 7C and Supplementary Figure S8A). In addition, the expression of TRF2 prevented further Sat III DNA loss, as seen by the higher intensity of Sat III DNA as compared to control cells (Supplementary Figure S8B). The hTERT-expressing post-senescent cells divide continuously with restored telomere length, TRF2 expression as well as PCH DNA stability, condensation and content (Figure 7D and Supplementary Figure S8C, S8D). These results can simply be interpreted as a reversal of the TP53-dependent TRF2 downregulation triggered by telomere shortening. Noteworthy, in the p21-compromised cells restarting to growth, there is a partial re-condensation and increased content of pericentromeric DNA (Figure 7D and Supplementary Figure S8B) while the TRF2 level remains low (Supplementary Figure S8D). Therefore, in these cells, there must be TRF2-independent mechanisms that partially restore pericentromere integrity (condensation and content) independently of the pericentromeric DNA damages that remain high in these cells. Nevertheless, TRF2 inhibition in hTERT cells leads to a pericentromeric decondensation, showing that in cells restarting to growth, the pericentromeric condensation is still, at least in part, under the control of TRF2.

Finally, using multicolor fluorescence in situ hybridization (M-FISH) in combination with inverted DAPI banding, we found chromosomal breakpoints in post-senescent cells (shp21^{CIP1} + Empty) preferentially involving heterochromatic ($P = 0.009$) and telomeric ($P = 006$) compared to euchromatic regions (Figure 7E and Supplementary Figure S8E). Notably, chromosomal aberrations involving heterochromatin regions were significantly reduced by TRF2 ($P = 0.004$) or hTERT ($P < 0.0001$) co-transductions while telomeric aberrations were significantly reduced by hTERT expression ($P = 0.001$).

These results show that in case of checkpoint failure and return to growth of senescent cells, the consequence of the PCH dismantling is the formation of chromosome rearrangements involving heterochromatin, a classical cytogenetic feature of human chromosome aberrations in cancer cells.

DISCUSSION

Here, we uncover a senescence mechanism driving heterochromatin dismantling in response to TP53 activation by downregulating the expression of the telomeric protein TRF2 (Figure 8). This reveals a new function of TP53 as a pericentromeric heterochromatin disassembler. Specifically, we found that the integrity of pericentromeric heterochromatin (PCH) is markedly and specifically altered in senescent cells, combining DNA damage, decondensation, elevated sister chromatid recombination, repetitive DNA loss and accumulation of cytosolic PCH DNA associated with cGAS. The PCH dismantling occurs when the cells enter into senescence and can be early detected in pre-senescent cultures. Its specificity is demonstrated by the preservation of the integrity of alphoid centromeric chromatin and other repeated heterochromatic regions when PCH becomes dismantled. We elucidated the mechanism driving these dramatic changes in heterochromatin integrity as being a consequence of TP53 activation leading to TRF2 downregulation and PCH dismantling. Indeed, the senescence-associated PCH dismantling phenotype can be prevented by TP53 inhibition or by an ectopic expression of TRF2 counteracting its TP53-dependent downregulation. Remarkably, the roughly half dosage of TRF2 induced by TP53 activation is sufficient to almost fully abolish its association with PCH DNA, in contrast to telomere binding that diminished by about 50%. This differential impact of the reduced TRF2 levels between telomeric and PCH DNA can be explained by the mass-action law principle, predicting that a limited variation in protein concentration has a greater impact on low-affinity binding sites, as expected for PCH DNA, than high-affinity sites, as telomeres. Hence, it is revealed that the TP53-dependent TRF2 downregulation exerts a more important impact on PCH stability than at telomeres. The fact that restoring the levels of TRF2 by TP53 inhibition in pre-senescent cells is not sufficient to rescue telomeric damage could be explained by the presence of critically short telomeres that can activate DDR.

These results highlight the biological importance of the role of the TRF2 association to heterochromatin, which we previously showed to be required for the progression of the replication fork through these difficult-to-replicate regions in transformed cells (31). Since PCH dismantling is already detected in presenescent cultures, the divisions of pre-senescent cells with a reduced level of TRF2 are likely to lead to the accumulation of PCH replicative damages as visualized by a reduced association of PCNA to PCH in presenescent cells. Of note, the PCH dismantling observed in bleomycin-treated cells also depends upon a TP53-dependent TRF2 downregulation and occurs in cell-cycle arrested cells due to the immediate checkpoint activation upon drug treatment. This implies that TRF2 must also have protective roles at PCH independently of replication. An explanation is that TRF2 has a general role in preventing ATM activation at PCH DSBs since TRF2 was reported to bind to accidental DSBs (43). The specific protection of PCH by TRF2 could also be related to the ability of TRF2 to regulate the formation of DNA/RNA hybrids (R-loops) (44,45) that are expected to accumulate at PCH in stressed cells (46). A PCH protective role of TRF2 both during replication and as part of the normal PCH DNA repair is supported by the finding that the PCH dismantling is not restored upon the overexpression of a truncated form of TRF2 lacking the basic N-terminal domain (TRF2$^{\Delta B}$), a mutant form previously reported to be impaired in both PCH replication (31) and DSB signaling (43).

The PCH dismantling triggered by TRF2 downregulation in senescent cells is ATM-dependent. This, to-

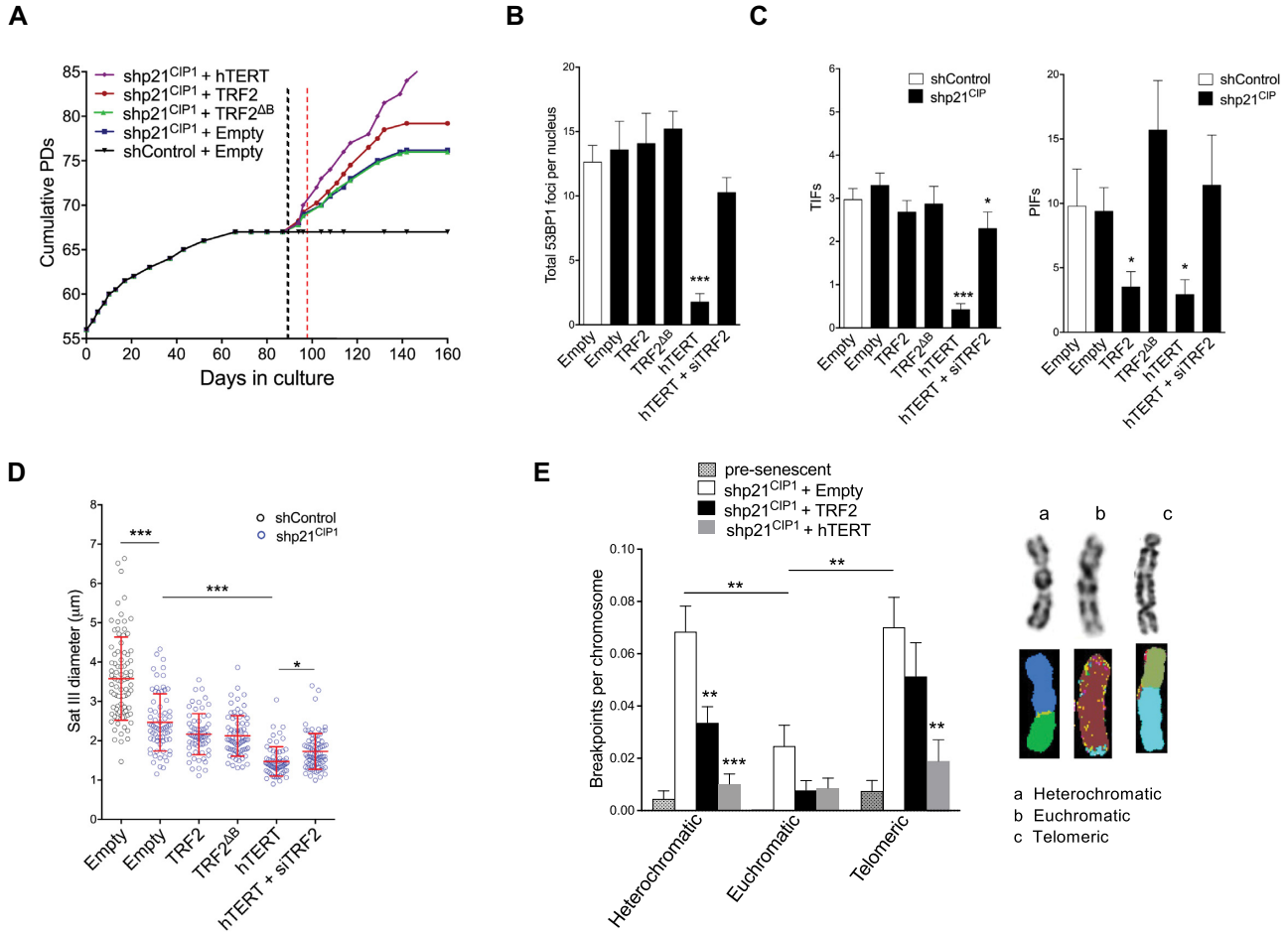

Figure 7. TRF2 is required for pericentromeric DNA stability in post-senescent cells. (**A**) Growth curve of senescence cells transduced with sh21CIP1 together with either empty, TRF2, TRF2ΔB or hTERT lentiviral vectors (black dotted line). Cells were collected 10 days post-infection (red dotted line). (**B**) Total damage, (**C**) TIFs, PIFs and (**D**) Sat III opening of the conditions described in A. TRF2 downregulation in hTERT expressing cells was carried out for three days using siRNAs. Data represent the mean ± SD of three biological replicates. Statistical analyses were performed using the Kruskal–Wallis test ($^{*}P < 0.01$; $^{***}P < 0.0001$). (**E**) Chromosome breakpoints quantification identified by Inverted-DAPI Banding and multicolor FISH. Examples show an heterochromatic [der(X)t(X;9)(q22.1;q11)], an euchromatic [der(7)t(2;7)] and a telomeric [dic(1;17)(pter;pter)] chromosome breakpoint. Error bars represent the mean ± SD of approximately 15 metaphases. Statistical analyses were performed using the Kruskal–Wallis test ($^{**}P < 0.001$; $^{***}P < 0.0001$).

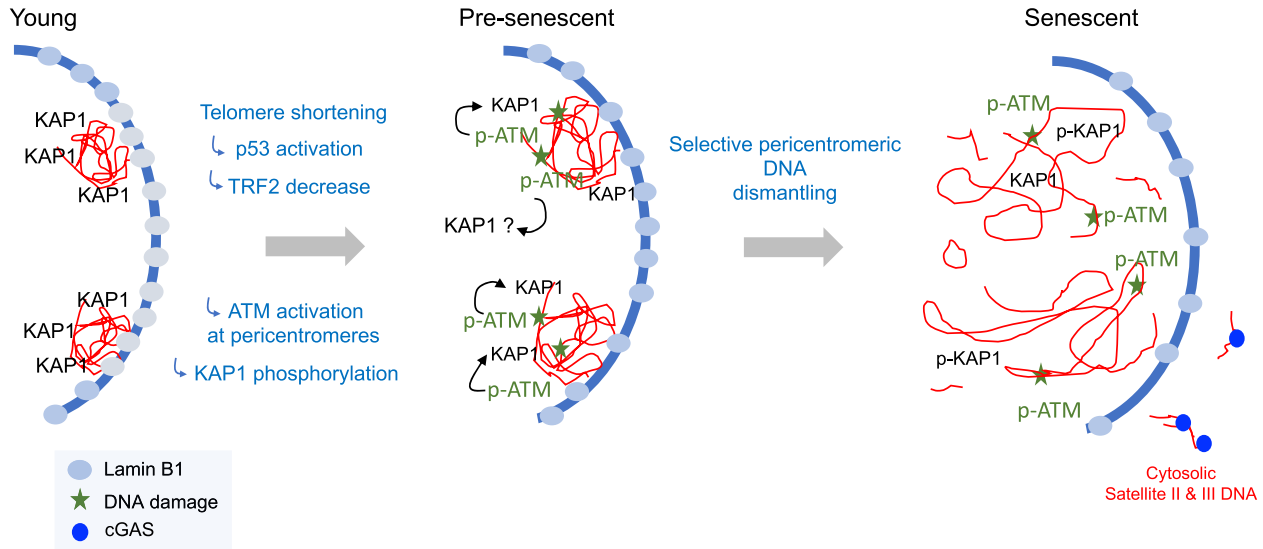

Figure 8. Model of pericentromeric DNA dismantling during cellular senescence.

gether with the fact that the association of KAP1 and LMNB1 at PCH is TRF2 and ATM-dependent, suggests that senescence-induced PCH decondensation involves the release of KAP1 and LMNB1 from these regions. The release of KAP1 and LMNB1 from PCH is not simply the consequence of general DDR generated by telomere shortening in replicative senescent cells, since expressing a TRF2 allele lacking its N-terminal domain leads to PCH deprotection but maintaining telomere stability (see Figure 5A–C). These results agree with the model that TRF2 downregulation leads to ATM-dependent phosphorylation of KAP1 at PCH DNA, leading to an overall decrease in the amount of KAP1 in this region. Overall, our results delineate the following model of how TP53 activation drives PCH dismantling. As a consequence of senescence stressors, such as telomere shortening or genotoxic exposure, TP53 activation decreases TRF2 expression, which triggers DNA damage selectively at PCH resulting in ATM activation. This leads to PCH decondensation through the release of KAP1 and LMNB1 (see the model in Figure 8). This is in agreement with the finding that KAP1 is phosphorylated by ATM in case of heterochromatin damage leading to local opening and repair (34,35). This also indicates that TRF2 controls the association of LMNB1 to PCH and might result from a direct TRF2-LMNB1 interaction that is currently under investigation (Mendez-Bermudez et al, unpublished) and previously suggested (47,48). Upon TRF2 downregulation, there is a substantial PCH dismantling leading to the assumption that the DNA damages are too important to be normally repaired. The resulting PCH decondensation and illegitimate repair are expected to lead to sister chromatid recombination events resulting in PCH DNA excision and accumulation in the cytoplasm.

The PCH dismantling due to TRF2 downregulation does not cause the entry into senescence since $TRF2^{\Delta B}$ overexpression does not rescue PCH dismantling while it is sufficient to bypass the senescence checkpoint, like full-length TRF2 (Figure 5A). This, together with our finding that telomere protection at the onset of replicative senescence is insensitive to global TRF2 dosage, suggests that TRF2 prevents replicative senescence arrest independently of its roles in telomere and PCH protection.

If the senescence-associated PCH dismantling does not cause cell cycle arrest at the onset of senescence, it plays other important roles in the senescence program. Indeed, we showed that PCH dismantling facilitates the activation of an interferon response by favoring the accumulation of cytosolic PCH DNA prone to activate the cGAS-STING pathway in a TRF2-dependent manner (Figure 6A). This might be due to the preferred binding of cGAS to Sat III DNA repeats (36). The fact that p53 knockdown leads to an overall increase in cytosolic DNA could be explained by the multiple roles of p53 on genome stability. Importantly, the proportion of cytosolic DNA containing PCH bound to cGAS decreased upon TP53 downregulation, an effect that is in agreement with the role of p53 on TRF2 degradation.

This mechanism appears distinct from the activation of the L1 retrotransposons leading to an interferon response in late senescent cells (9) since the dismantling phenotype triggered by TRF2 downregulation occurs earlier, at senescence onset, and we did not detect an effect of TRF2 downregulation on L1 integrity. We also unveiled that PCH dismantling can result in aberrant heterochromatin rearrangements in case of senescence checkpoint failure. This suggests that aging, by generating senescence-associated PCH dismantling, favors, in case of checkpoint failure, complex chromosome rearrangements associated with cancer, providing a novel mechanism linking cell senescence to oncogenesis.

We discover here how the activation of TP53 in response to telomere shortening or genotoxic stress leads to a profound dismantling of the PCH compartment of our genome via the downregulation of the key telomere protein TRF2. This TP53–TRF2-axis is likely to play an important role during aging since we observed age-dependent signs of selective PCH dismantling in various human cell types, including MSCs and skin fibroblasts. We anticipate that interventions stabilizing TRF2 will prevent heterochromatin dismantling during aging thus offering a valuable strategy to prevent age-related diseases, including cancer.

DATA AVAILABILITY

ChIP-seq raw data is available in the Sequence Read Archive (SRA) repository accession code PRJNA674763. RNA-seq data were deposited in the Gene Expression Omnibus database under accession number GSE160503.

SUPPLEMENTARY DATA

Supplementary Data are available at NAR Online.

ACKNOWLEDGEMENTS

We thank Dr Sara Selig for her advice on Satellite II Southern blotting. The IRCAN's Molecular and Cellular Core Imaging (PICMI) is supported by 'le Cancéropole PACA, la Région Provence Alpes-Côte d'Azur, le Conseil Départemental 06' and INSERM. The IRCAN's GenoMed, the Genomic Core Facility at IRCAN is supported by le Conseil Départemental 06, Aviesan and INSERM.

FUNDING

INSERM program on aging (AGEMED), "Investments for the Future" LABEXSIGNALIFE [ANR-11-LABX-0028-01]; 'Fondation ARC pour la recherche contre le cancer', INCa [project REPLITOP] and the ANR [projects TELOCHROM and S-ENCODE]; work in the J.Y. laboratory was supported by the National Natural Science Foundation of China [81971312, 91749126, 81911530241, 81871549, 81671900]; Program of Shanghai Academic/Technology Research Leader [19XD1422500]; Shanghai Municipal Education Commission [Oriental Scholars Program, 2019]. Funding for open access charge: Public funding.
Conflict of interest statement. None declared.

REFERENCES

1. Kennedy,B.K., Berger,S.L., Brunet,A., Campisi,J., Cuervo,A.M., Epel,E.S., Franceschi,C., Lithgow,G.J., Morimoto,R.I., Pessin,J.E. *et al.* (2014) Geroscience: linking aging to chronic disease. *Cell*, **159**, 709–713.

2. Gorgoulis,V., Adams,P.D., Alimonti,A., Bennett,D.C., Bischof,O., Bishop,C., Campisi,J., Collado,M., Evangelou,K., Ferbeyre,G. *et al.* (2019) Cellular senescence: defining a path forward. *Cell*, **179**, 813–827.
3. Narita,M., Nunez,S., Heard,E., Lin,A.W., Hearn,S.A., Spector,D.L., Hannon,G.J. and Lowe,S.W. (2003) Rb-mediated heterochromatin formation and silencing of E2F target genes during cellular senescence. *Cell*, **113**, 703–716.
4. Zhang,W., Li,J., Suzuki,K., Qu,J., Wang,P., Zhou,J., Liu,X., Ren,R., Xu,X., Ocampo,A. *et al.* (2015) Aging stem cells. A werner syndrome stem cell model unveils heterochromatin alterations as a driver of human aging. *Science*, **348**, 1160–1163.
5. Swanson,E.C., Manning,B., Zhang,H. and Lawrence,J.B. (2013) Higher-order unfolding of satellite heterochromatin is a consistent and early event in cell senescence. *J. Cell. Biol.*, **203**, 929–942.
6. De Cecco,M., Criscione,S.W., Peckham,E.J., Hillenmeyer,S., Hamm,E.A., Manivannan,J., Peterson,A.L., Kreiling,J.A., Neretti,N. and Sedivy,J.M. (2013) Genomes of replicatively senescent cells undergo global epigenetic changes leading to gene silencing and activation of transposable elements. *Aging Cell*, **12**, 247–256.
7. Nishibuchi,G. and Dejardin,J. (2017) The molecular basis of the organization of repetitive DNA-containing constitutive heterochromatin in mammals. *Chromosome Res.*, **25**, 77–87.
8. Freund,A., Laberge,R.M., Demaria,M. and Campisi,J. (2012) Lamin B1 loss is a senescence-associated biomarker. *Mol. Biol. Cell.*, **23**, 2066–2075.
9. De Cecco,M., Ito,T., Petrashen,A.P., Elias,A.E., Skvir,N.J., Criscione,S.W., Caligiana,A., Brocculi,G., Adney,E.M., Boeke,J.D. *et al.* (2019) L1 drives IFN in senescent cells and promotes age-associated inflammation. *Nature*, **566**, 73–78.
10. Simon,M., Van Meter,M., Ablaeva,J., Ke,Z., Gonzalez,R.S., Taguchi,T., De Cecco,M., Leonova,K.I., Kogan,V., Helfand,S.L. *et al.* (2019) LINE1 derepression in aged wild-type and SIRT6-Deficient mice drives inflammation. *Cell Metab*, **29**, 871–885.
11. Hu,H., Ji,Q., Song,M., Ren,J., Liu,Z., Wang,Z., Liu,X., Yan,K., Hu,J., Jing,Y. *et al.* (2020) ZKSCAN3 counteracts cellular senescence by stabilizing heterochromatin. *Nucleic Acids Res.*, **48**, 6001–6018.
12. Deng,L., Ren,R., Liu,Z., Song,M., Li,J., Wu,Z., Ren,X., Fu,L., Li,W., Zhang,W. *et al.* (2019) Stabilizing heterochromatin by DGCR8 alleviates senescence and osteoarthritis. *Nat. Commun.*, **10**, 3329.
13. Williams,E.S. and Bailey,S.M. (2009) Chromosome orientation fluorescence in situ hybridization (CO-FISH). *Cold Spring Harb Protoc.*, **2009**, pdb prot5269.
14. Rai,T.S. and Adams,P.D. (2016) ChIP-Sequencing to map the epigenome of senescent cells using benzonase endonuclease. *Methods Enzymol.*, **574**, 355–364.
15. Chen,S., Zhou,Y., Chen,Y. and Gu,J. (2018) fastp: an ultra-fast all-in-one FASTQ preprocessor. *Bioinformatics*, **34**, i884–i890.
16. Langmead,B. and Salzberg,S.L. (2012) Fast gapped-read alignment with bowtie 2. *Nat. Methods*, **9**, 357–359.
17. Stovner,E.B. and Saetrom,P. (2019) epic2 efficiently finds diffuse domains in chip-seq data. *Bioinformatics*, **35**, 4392–4393.
18. Amemiya,H.M., Kundaje,A. and Boyle,A.P. (2019) The ENCODE blacklist: identification of problematic regions of the genome. *Sci. Rep.*, **9**, 9354.
19. Bolger,A.M., Lohse,M. and Usadel,B. (2014) Trimmomatic: a flexible trimmer for illumina sequence data. *Bioinformatics*, **30**, 2114–2120.
20. Dobin,A., Davis,C.A., Schlesinger,F., Drenkow,J., Zaleski,C., Jha,S., Batut,P., Chaisson,M. and Gingeras,T.R. (2013) STAR: ultrafast universal RNA-seq aligner. *Bioinformatics*, **29**, 15–21.
21. Love,M.I., Huber,W. and Anders,S. (2014) Moderated estimation of fold change and dispersion for RNA-seq data with DESeq2. *Genome. Biol.*, **15**, 550.
22. d'Adda di Fagagna,F., Reaper,P.M., Clay-Farrace,L., Fiegler,H., Carr,P., Von Zglinicki,T., Saretzki,G., Carter,N.P. and Jackson,S.P. (2003) A DNA damage checkpoint response in telomere-initiated senescence. *Nature*, **426**, 194–198.
23. Beliveau,A., Bassett,E., Lo,A.T., Garbe,J., Rubio,M.A., Bissell,M.J., Campisi,J. and Yaswen,P. (2007) p53-dependent integration of telomere and growth factor deprivation signals. *Proc. Natl. Acad. Sci. U.S.A.*, **104**, 4431–4436.
24. Valgardsdottir,R., Chiodi,I., Giordano,M., Rossi,A., Bazzini,S., Ghigna,C., Riva,S. and Biamonti,G. (2008) Transcription of satellite III non-coding RNAs is a general stress response in human cells. *Nucleic Acids Res.*, **36**, 423–434.
25. Pal,S., Postnikoff,S.D., Chavez,M. and Tyler,J.K. (2018) Impaired cohesion and homologous recombination during replicative aging in budding yeast. *Sci. Adv.*, **4**, eaaq0236.
26. Fumagalli,M., Rossiello,F., Clerici,M., Barozzi,S., Cittaro,D., Kaplunov,J.M., Bucci,G., Dobreva,M., Matti,V., Beausejour,C.M. *et al.* (2012) Telomeric DNA damage is irreparable and causes persistent DNA-damage-response activation. *Nat. Cell. Biol.*, **14**, 355–365.
27. Hewitt,G., Jurk,D., Marques,F.D., Correia-Melo,C., Hardy,T., Gackowska,A., Anderson,R., Taschuk,M., Mann,J. and Passos,J.F. (2012) Telomeres are favoured targets of a persistent DNA damage response in ageing and stress-induced senescence. *Nat. Commun.*, **3**, 708.
28. Grolimund,L., Aeby,E., Hamelin,R., Armand,F., Chiappe,D., Moniatte,M. and Lingner,J. (2013) A quantitative telomeric chromatin isolation protocol identifies different telomeric states. *Nat. Commun.*, **4**, 2848.
29. Fujita,K., Horikawa,I., Mondal,A.M., Jenkins,L.M., Appella,E., Vojtesek,B., Bourdon,J.C., Lane,D.P. and Harris,C.C. (2010) Positive feedback between p53 and TRF2 during telomere-damage signalling and cellular senescence. *Nat. Cell. Biol.*, **12**, 1205–1212.
30. Wei,W., Hemmer,R.M. and Sedivy,J.M. (2001) Role of p14(ARF) in replicative and induced senescence of human fibroblasts. *Mol. Cell. Biol.*, **21**, 6748–6757.
31. Mendez-Bermudez,A., Lototska,L., Bauwens,S., Giraud-Panis,M.J., Croce,O., Jamet,K., Irizar,A., Mowinckel,M., Koundrioukoff,S., Nottet,N. *et al.* (2018) Genome-wide control of heterochromatin replication by the telomere capping protein TRF2. *Mol. Cell.*, **70**, 449–461.
32. Karlseder,J., Smogorzewska,A. and de Lange,T. (2002) Senescence induced by altered telomere state, not telomere loss. *Science*, **295**, 2446–2449.
33. Bauwens,S., Lototska,L., Koundrioukoff,S., Debatisse,M., Ye,J., Gilson,E. and Mendez-Bermudez,A. (2021) The telomeric protein TRF2 regulates replication origin activity within pericentromeric heterochromatin. *Life (Basel)*, **11**, 267.
34. Ziv,Y., Bielopolski,D., Galanty,Y., Lukas,C., Taya,Y., Schultz,D.C., Lukas,J., Bekker-Jensen,S., Bartek,J. and Shiloh,Y. (2006) Chromatin relaxation in response to DNA double-strand breaks is modulated by a novel ATM- and KAP-1 dependent pathway. *Nat. Cell. Biol.*, **8**, 870–876.
35. Goodarzi,A.A., Noon,A.T., Deckbar,D., Ziv,Y., Shiloh,Y., Lobrich,M. and Jeggo,P.A. (2008) ATM signaling facilitates repair of DNA double-strand breaks associated with heterochromatin. *Mol. Cell.*, **31**, 167–177.
36. Gentili,M., Lahaye,X., Nadalin,F., Nader,G.P.F., Puig Lombardi,E., Herve,S., De Silva,N.S., Rookhuizen,D.C., Zueva,E., Goudot,C. *et al.* (2019) The N-Terminal domain of cGAS determines preferential association with centromeric DNA and innate immune activation in the nucleus. *Cell Rep.*, **26**, 2377–2393.
37. Campisi,J. and d'Adda di Fagagna,F. (2007) Cellular senescence: when bad things happen to good cells. *Nat. Rev. Mol. Cell. Biol.*, **8**, 729–740.
38. Bignell,G.R., Greenman,C.D., Davies,H., Butler,A.P., Edkins,S., Andrews,J.M., Buck,G., Chen,L., Beare,D., Latimer,C. *et al.* (2010) Signatures of mutation and selection in the cancer genome. *Nature*, **463**, 893–898.
39. Beroukhim,R., Mermel,C.H., Porter,D., Wei,G., Raychaudhuri,S., Donovan,J., Barretina,J., Boehm,J.S., Dobson,J., Urashima,M. *et al.* (2010) The landscape of somatic copy-number alteration across human cancers. *Nature*, **463**, 899–905.
40. Sawyer,J.R., Tian,E., Heuck,C.J., Epstein,J., Johann,D.J., Swanson,C.M., Lukacs,J.L., Johnson,M., Binz,R., Boast,A. *et al.* (2014) Jumping translocations of 1q12 in multiple myeloma: a novel mechanism for deletion of 17p in cytogenetically defined high-risk disease. *Blood*, **123**, 2504–2512.
41. Gagos,S., Chiourea,M., Christodoulidou,A., Apostolou,E., Raftopoulou,C., Deustch,S., Jefford,C.E., Irminger-Finger,I., Shay,J.W. and Antonarakis,S.E. (2008) Pericentromeric instability and spontaneous emergence of human neoacrocentric and minute chromosomes in the alternative pathway of telomere lengthening. *Cancer Res.*, **68**, 8146–8155.

42. Lototska,L., Yue,J.X., Li,J., Giraud-Panis,M.J., Songyang,Z., Royle,N.J., Liti,G., Ye,J., Gilson,E. and Mendez-Bermudez,A. (2020) Human RAP1 specifically protects telomeres of senescent cells from DNA damage. *EMBO Rep.*, **21**, e49076.
43. Bradshaw,P.S., Stavropoulos,D.J. and Meyn,M.S. (2005) Human telomeric protein TRF2 associates with genomic double-strand breaks as an early response to DNA damage. *Nat. Genet.*, **37**, 193–197.
44. Lee,Y.W., Arora,R., Wischnewski,H. and Azzalin,C.M. (2018) TRF1 participates in chromosome end protection by averting TRF2-dependent telomeric r loops. *Nat. Struct. Mol. Biol.*, **25**, 147–153.
45. Tan,J., Duan,M., Yadav,T., Phoon,L., Wang,X., Zhang,J.M., Zou,L. and Lan,L. (2020) An R-loop-initiated CSB-RAD52-POLD3 pathway suppresses ROS-induced telomeric DNA breaks. *Nucleic Acids Res.*, **48**, 1285–1300.
46. Jolly,C., Metz,A., Govin,J., Vigneron,M., Turner,B.M., Khochbin,S. and Vourc'h,C. (2004) Stress-induced transcription of satellite III repeats. *J. Cell. Biol.*, **164**, 25–33.
47. Pennarun,G., Picotto,J., Etourneaud,L., Redavid,A.R., Certain,A., Gauthier,L.R., Fontanilla-Ramirez,P., Busso,D., Chabance-Okumura,C., Theze,B. *et al.* (2021) Increase in lamin B1 promotes telomere instability by disrupting the shelterin complex in human cells. *Nucleic Acids Res.*, **49**, 9886–9905.
48. Rendon-Gandarilla,F.J., Alvarez-Hernandez,V., Castaneda-Ortiz,E.J., Cardenas-Hernandez,H., Cardenas-Guerra,R.E., Valdes,J., Betanzos,A., Chavez-Munguia,B., Lagunes-Guillen,A., Orozco,E. *et al.* (2018) Telomeric repeat-binding factor homologs in entamoeba histolytica: new clues for telomeric research. *Front. Cell Infect. Microbiol.*, **8**, 341.